ACS NANO

www.acsnano.org

ARTICLE

Contact-Resistance-Free Stretchable Strain Sensors with High Repeatability and Linearity

Shuang Li, Guodong Liu, Rui Li, Qinlan Li, Yang Zhao, Mingqi Huang, Maoyi Zhang, Shizhen Yin, Yixin Zhou, Hao Tang, Liwu Wang, Guanhui Fang, and Yewang Su*

Cite This: *ACS Nano* 2022, 16, 541−553

Read Online

ACCESS | Metrics & More | Article Recommendations | Supporting Information

ABSTRACT: **Most of the existing stretchable strain sensors are based on the contact-resistance mechanism, where the stretchability and resistance variation depend on the change of the contact relationship of the conductive microstructures. These sensors usually exhibit large sensing ranges and gauge factors but unsatisfactory repeatability and linearity of the electrical responses because the contact is unstable. Here, we report a completely different design for stretchable strain sensors based on a contact-resistance-free structure, i.e., the off-axis serpentine sandwich structure (OASSS), with the mechanism of the stretch−bending−stretch transformation (SBST). Neither unstable contact resistance nor nonlinear constitutive and geometric behaviors occur for the OASSS while the sensor undergoes a large applied strain (50%), which guarantees high repeatability (repeatability error = 1.58%) and linearity (goodness-of-fit >0.999). Owing to such performances, the present sensors are not only applied to monitoring human activities and medical surgery but also to the ground tests of Tianwen-1, China's first Mars exploration mission.**

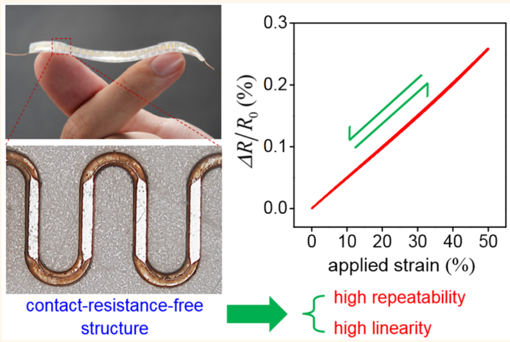

KEYWORDS: *flexible electronics, stretchable strain sensors, high repeatability, high linearity, Tianwen-1*

Flexible electronics integrated with various sensors, including strain sensors,[1−4] bending curvature sensors,[5,6] pressure sensors,[7,8] temperature sensors,[9,10] pulse sensors,[10,11] blood oxygen sensors,[12,13] ultrasonic transducers,[14] hydrogen sensors,[15] artificial compound eyes,[16,17] *etc.*, have been rapidly developed in recent years. The applications range from health monitoring, medical treatment, the intelligence industry, to flexible and stretchable aerospace equipment. Strain sensors with large sensing ranges are key components for monitoring the deformation in these applications. However, traditional strain sensors based on metals or semiconductors, which are ubiquitous in rigid engineering systems, cannot meet the basic requirements of conformal fit with human bodies or flexible equipment, and they usually exhibit narrow sensing ranges (less than 5%)[9,18] while the actual demand is much higher.[19,20] Practical applications require the following performances of a stretchable strain sensor. (1) Large sensing range. The maximum strain in the human body under various postures and activities can reach 50%,[21,22] and thus, the sensing range is recommended to reach 50% or more. (2) High repeatability. The high repeatability of response curves for a sensor under continuous loading and unloading is essential for accurate sensing.[23] (3) High linearity.[18,23−27] When installing the sensor onto a sensing target such as the human skin, practical operation usually cannot ensure that the installing regime of the sensor is strain-free. The operation of zero clearing must be applied. High linearity is required such that the sensing results do not depend on the installing regime of the sensor and the operation of zero clearing (details shown in Figure S1 and the text in the Supporting Information). (4) Appropriate gauge factor (GF). An appropriate GF is required to guarantee the resolution.[27] (5) High temperature insensitivity. The sensing results should be insensitive to the temperatures of the environment and the sensing target.[28] (6) Low hysteresis. Low hysteresis is required for accurate monitoring of the activities of the sensing target.

Plenty of research has been devoted to new-type stretchable strain sensors, which usually exhibit large sensing ranges and GFs but unsatisfactory repeatability and linearity of the electrical responses,[5,29,30] although all of them are particularly important for practical applications.[18,26] The mainstream

Received: September 1, 2021
Accepted: December 14, 2021
Published: December 17, 2021

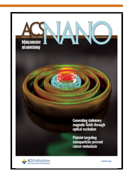

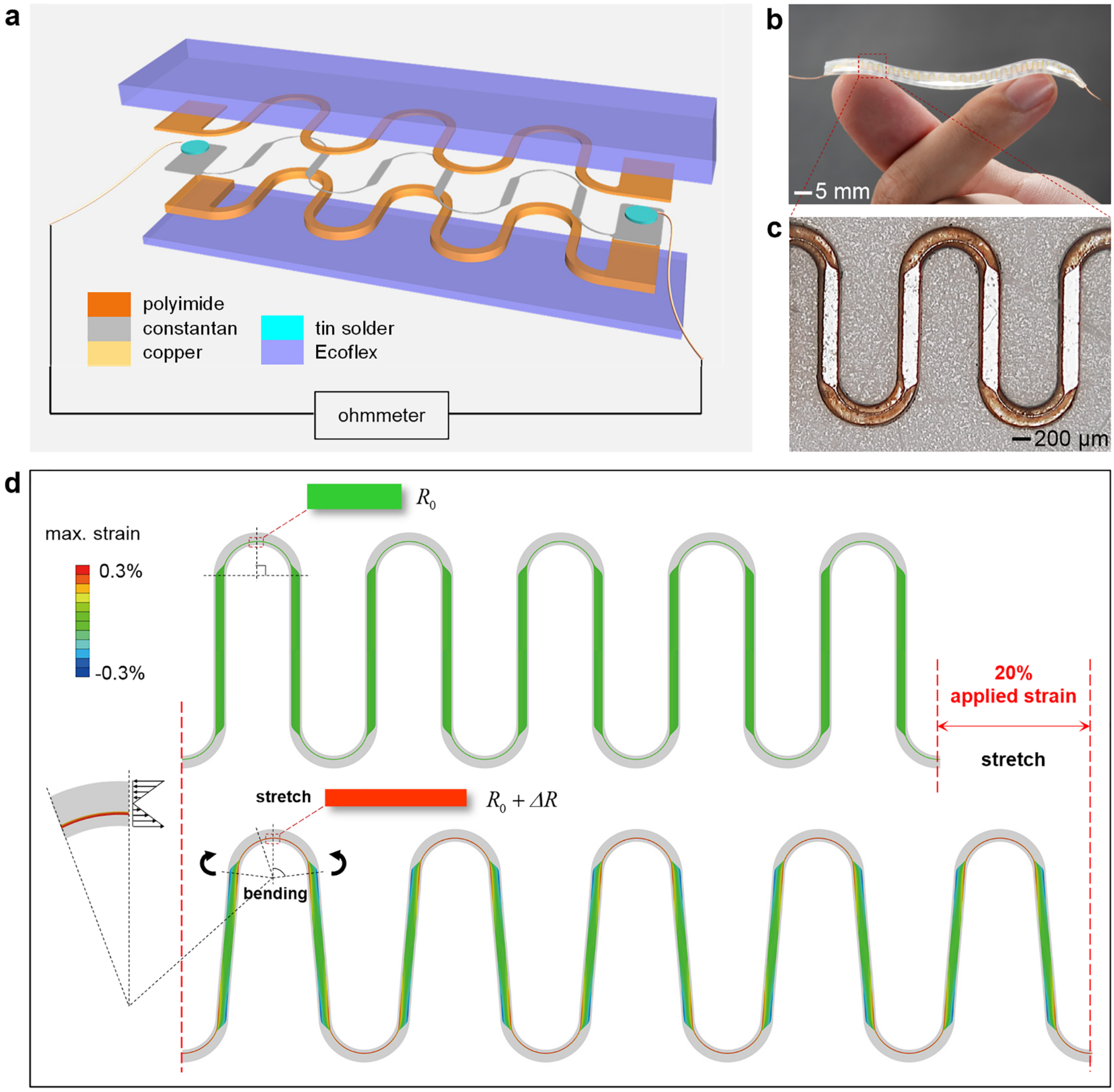

Figure 1. Schematic illustrations and images of a contact-resistance-free stretchable strain sensor. (a) Illustration of the contact-resistance-free sensor and its measurement scheme. Orange, polyimide; gray, constantan; light yellow, copper; aqua green, tin solder; light blue, Ecoflex. (b) Optical image of a fabricated strain sensor. (c) 3D digital microscopy image of the off-axis serpentine constantan foil and the serpentine PI substrate. (d) Schematic illustration of the sensing mechanism.

strategy of the existing research on stretchable strain sensors is to make use of the contact-resistance mechanism, where the stretchability and resistance variation depend on the change of the contact relationship (from contact to separation or from very close to far away involving the percolation effect or tunneling effect) of the conductive microstructures, which can be implemented by a variety of sensing materials and corresponding microstructure designs. Carbon-based materials, including carbon nanotubes,[29−32] grapheme,[5,33−39] carbonized silk,[40] carbon black,[41,42] *etc.*, are frequently used for the sensing materials of stretchable strain sensors. Other materials such as metal nanowires[18,43,44] and ZnO nanowires[45] are also adopted to fabricate stretchable strain sensors. The corresponding microstructures include the spring-like structure,[5] island-gap structure,[30,40] buckled sheath-core fiber-based structure,[33] fish-scale-like structure,[39] prestrained anisotropic network structure,[44] *etc.* The reason for unsatisfactory repeatability and linearity can be summarized as follows. Because of the unstable contact involving complicated slippage, friction, and adhesion among these inner surfaces, nonlinear deformation of the microstructures, and contact mode conversion, the repeatability and the linearity between the applied strain and the electrical response usually cannot be guaranteed during large deformation of the sensors.

In this work, we report a design for stretchable strain sensors based on a microfabricated contact-resistance-free structure, which is completely different from the strategy of the contact-resistance mechanism. Here, the terms "contact-resistance" and "contact-resistance-free" both refer to the sensing part of the sensor, not involving the interface between the sensing part

https://doi.org/10.1021/acsnano.1c07645
ACS Nano 2022, 16, 541−553

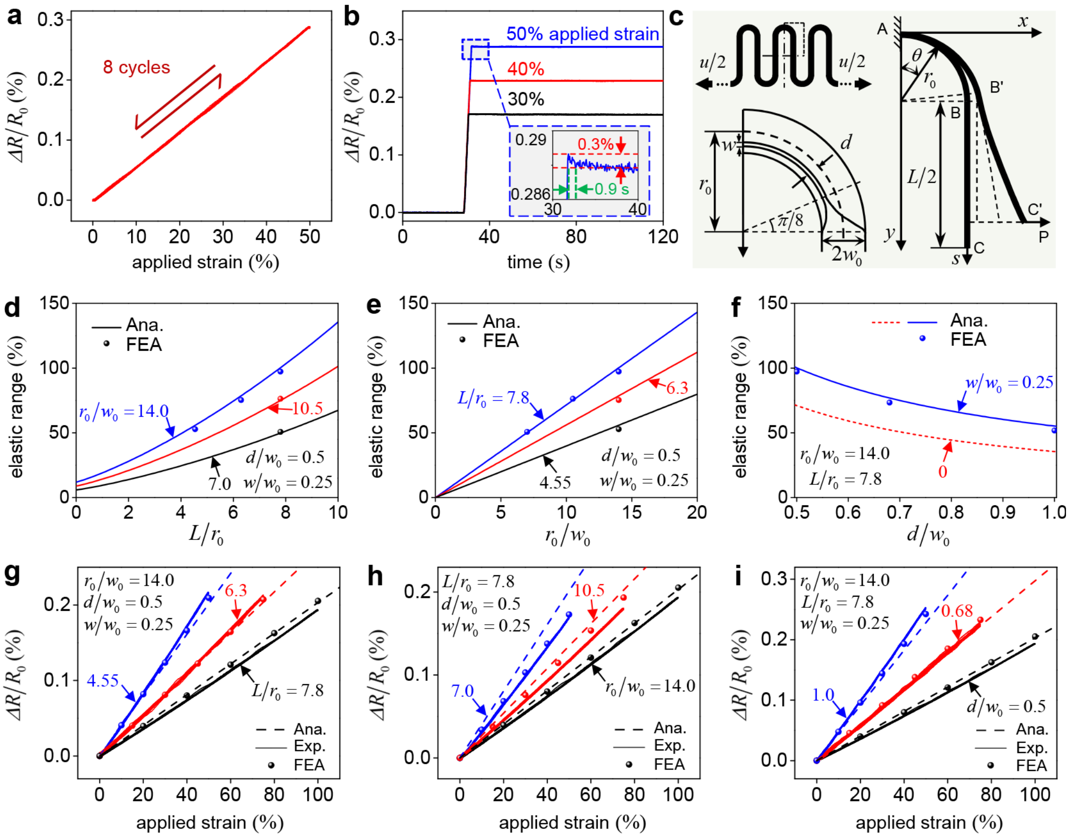

Figure 2. Mechanical and electrical characterization of the OASSS. (a) Relative resistance change of the OASSS *versus* the applied strain for eight consecutive loading−unloading cycles (applied strain of 0−50%). (b) Relative resistance changes for a step strain (strain rate 14% s^{-1}) from 0% to 30%/40%/50%. Inset: close-up of the overshoot of about 0.3%. (c) Mechanical model of the OASSS. Top left: the OASSS with multiple periods under horizontal stretch. Right: a quarter period of the structure in the initial stress-free state and the deformed state. Bottom left: geometric details of the arc segment. (d) Curves of the elastic range *versus* L/r_0 for the OASSSs with d/w_0 = 0.5, w/w_0 = 0.25, and r_0/w_0 = 7.0, 10.5, and 14.0. (e) Curves of the elastic range *versus* r_0/w_0 for the OASSSs with d/w_0 = 0.5, w/w_0 = 0.25, and L/r_0 = 4.55, 6.3, and 7.8. (f) Curves of the elastic range *versus* d/w_0 for the OASSSs with r_0/w_0 = 14.0, L/r_0 = 7.8, and w/w_0 = 0 and 0.25. Relative resistance changes of the OASSSs *versus* the applied strain for eight consecutive loading−unloading cycles: (g) r_0/w_0 = 14.0, d/w_0 = 0.5, w/w_0 = 0.25, and L/r_0 = 4.55, 6.3, and 7.8; (h) L/r_0 = 7.8, d/w_0 = 0.5, w/w_0 = 0.25, and r_0/w_0 = 7.0, 10.5, and 14.0; (i) r_0/w_0 = 14.0, L/r_0 = 7.8, w/w_0 = 0.25, and d/w_0 = 0.5, 0.68, and 1.0.

and the lead wire where the contact resistance does not change during the measurement. The stretchable strain sensor is composed of an off-axis serpentine sandwich structure (OASSS) and encapsulation layers. A large sensing range is accomplished based on the mechanism of the stretch−bending−stretch transformation (SBST), where only the geometric change of the conductive material is used to realize the change in resistance. High repeatability and linearity are guaranteed because neither unstable contact resistance nor nonlinear constitutive and geometric behaviors occur during the sensing process. A design of temperature self-compensation is developed taking advantage of the OASSS and the Wheatstone bridge circuit. The present sensors are applied not only to monitoring human activities and medical surgery but also to the ground tests of Tianwen-1, China's first Mars exploration mission. The design idea of contact-resistance-free structures and the OASSS can be extended to stretchable strain sensors with high accuracy and other special advantages by employing different functional materials, such as silver nanowires for transparency, gold film for chemical stability, and biodegradable materials for reducing environmental pollution or the harm to organisms.

RESULTS AND DISCUSSION

Design, Fabrication, and Mechanism. Figure 1a illustrates the multilayer configuration of the contact-resistance-free stretchable strain sensor, consisting of an OASSS and the bottom and top encapsulation layers (Ecoflex 00-30, Smooth-On, USA). The OASSS is composed of an off-axis serpentine conductive foil (constantan foil in this work) with two external leads via the corresponding tin solders, a thick serpentine polyimide (PI) substrate, and a thin serpentine PI cover layer, where the axis of the constantan foil is off the axes of the PI substrate and cover layer. Here, constantan is used as the sensing material because of its low resistance temperature coefficient (~10^{-6} °C^{-1}), which helps to reduce the effect of the ambient temperature. The PI cover layer is to enhance the bonding between the constantan foil and the PI substrate. The fabrication process of the sensor is outlined in Figure S2, which is realized by standard planar microfabrication strategies, including spin coating, lithography, laser cutting, and encapsulation. Details are shown in the Experimental Section. Figure 1b and Figure S3 show the super flexibility of a fabricated strain sensor, with the image of a 3D digital microscope (RH-8800, HiRox, Japan) given in Figure

1c for the off-axis serpentine constantan foil and the serpentine PI substrate.

The sensing mechanism is understood by the SBST (Figure 1d). The OASSS is subjected to a stretching (S) applied strain when the sensor follows the deformation of the sensing target. Because the PI substrate is thick relative to the width, the OASSS almost undergoes in-plane deformation without out-of-plane buckling.[46] The in-plane bending (B) of the arc segments and the rotation of the straight segments dominate the deformation of the OASSS.[47] The maximum strain occurs in the arc segments, while the deformation in the straight segments is much smaller. Therefore, a narrow off-axis layout design is achieved for the arc segments of the constantan foil compared with the wide layout for the straight segments. The stretching applied strain is transferred, via the bending of the arc segment, to the narrow off-axis constantan foil with a stretch (S) strain, of which the resistance change can be detected by connecting the leads to an ohmmeter.

Mechanical and Electrical Characterization of the OASSS. The characterization of the OASSS dominates the performance of the stretchable strain sensor. Figure 2a shows the experimental results on the relationship between the relative resistance change $\Delta R/R_0$ and the applied strain $\varepsilon_{\text{applied}}$ of an OASSS (detailed layouts shown in Figure S4) for eight consecutive loading−unloading cycles (details shown in the Experimental Section and Figure S6). For the applied strain of 0−50%, the relationship exhibits extremely high repeatability, with the repeatability error[26] δ_{R} = 0.9979%, and high linearity, with the goodness-of-fit R^2 ranging from 0.99974 to 0.99995 for the 8 cycles. Here, R_0 and ΔR represent the original resistance of the OASSS and its increment due to the applied strain, respectively. Another important advantage of the OASSS is the good dynamic response, as shown in Figure 2b. When a 50% strain is applied at a strain rate of 14% s^{-1}, only 0.3% overshoot occurs with a short recovery time of 0.9 s. The performances of the OASSS, which will hold for the stretchable strain sensors with encapsulation layers, are attributed to the contact-resistance-free structures. Each material point of the OASSS deforms along a certain path during the consecutive loading−unloading cycles, which ensures the repeatability of the electrical response. This is the key difference from the existing stretchable strain sensors based on the contact-resistance mechanism. On the other hand, these performances are also attributed to the off-axis layout design. As shown in Figure S7, a conventional sandwich serpentine structure, with the same design of the serpentine PI substrate as that of the OASSS in Figure 2a but without the off-axis layout design, yields an irregular electrical response, which is not an optimal strategy for stretchable strain sensors.

In order to quantitatively analyze the effects of the design parameters and to optimize the design strategy, a mechanical model is established for the OASSS, as depicted in Figure 2c. The top-left subgraph illustrates an OASSS with multiple periods subjected to the applied strain. A quarter of one period (the right subgraph), consisting of a quarter of the arc segment with the radius r_0 and a straight segment with the length $L/2$, is analyzed according to the symmetry. The configuration ABC moves to AB′C′ when the left end A is fixed and the bottom end C/C′ is under an applied stretch. The width of the PI substrate and the PI cover is always a constant $2w_0$, while the width of the constantan foil remains a constant w in the top $3\pi/8$ arc segment (the bottom-left subgraph), transits smoothly to $2w_0$ in the remaining $\pi/8$ arc segment, and remains a constant $2w_0$ in the straight segment. The distance d from the inner edge of the constantan foil to the central axis of the PI layers remains constant in the top $3\pi/8$ arc segment as well. Considering the geometric character and the deformation mode, the OASSS is treated as the Euler−Bernoulli beam with variable stiffness.[47] The relationship between the applied strain $\varepsilon_{\text{applied}}$ and the maximum strain $\varepsilon_{\text{con,max}}$ of the constantan foil is obtained analytically as (details shown in Figure S8 and the text in the Supporting Information):

$$\varepsilon_{\text{applied}} = \frac{\overline{r}_0}{\overline{d} - \overline{a} - (I_{zr}/I_{rr})(\overline{h}_{\text{PI}}/2 - \overline{b})}\left(\frac{\overline{EI}_{z,\text{arc}}}{\overline{EI}_{z,\text{str}}}\frac{\overline{L}^3}{12\overline{L} + 24} + \frac{\pi\overline{L}^2 + 8\overline{L} + 2\pi}{4\overline{L} + 8}\right)\varepsilon_{\text{con,max}} \quad (1)$$

Here, $\overline{L} = L/r_0$, $\overline{r}_0 = r_0/w_0$, $\overline{d} = d/w_0$, and $\overline{h}_{\text{PI}} = h_{\text{PI}}/w_0$ are the dimensionless geometric parameters, $\overline{EI}_{z,\text{arc}}$ and $\overline{EI}_{z,\text{str}}$ are the bending stiffnesses of the arc segment and the straight segment, $(\overline{a} = a/w_0,\ \overline{b} = b/w_0)$ is the dimensionless position of the modulus-weighted centroid, and I_{rr} and I_{zr} are the modulus-weighted moments of inertia and the modulus-weighted product of inertia for the cross section of the arc segment, respectively. With the dimensionless thicknesses $\overline{h}_{\text{PI}} = h_{\text{PI}}/w_0 = 2.6$ for the PI substrate, $\overline{h}_{\text{con}} = h_{\text{con}}/w_0 = 0.05$ for the constantan foil, and the elastic limit $\varepsilon_{\text{con,max}} = 0.3\%$ for the constantan foil, the effects of the parameters $\overline{L}$, $\overline{r}_0$, $\overline{d}$, and $\overline{w} = w/w_0$ on the applied strain $\varepsilon_{\text{applied}}$, *i.e.*, the elastic range, are studied in Figure 2d−f, according to eq 1. With the constant $\overline{d}$ = 0.5 and $\overline{w}$ = 0.25, Figure 2d and e shows that the elastic sensing range increases monotonously with the increase of $\overline{L}$ and $\overline{r}_0$ for $\overline{r}_0$ = 7.0, 10.5, and 14.0 and $\overline{L}$ = 4.55, 6.3, and 7.8, respectively. On the other hand, the elastic sensing range decreases monotonously with the increase of $\overline{d}$ under $\overline{r}_0$ = 14.0 and $\overline{L}$ = 7.8 (Figure 2f). The elastic sensing range for $\overline{w}$ = 0.25 is larger than that for $\overline{w} \to 0$, because the position of the neutral axis is affected by the width of the constantan foil. These analytic results are verified by the finite element analysis (FEA, details shown in the Experimental Section) with seven sets of geometric parameters (Figure 2d−f), which correspond to approximately 50%, 75%, and 100% elastic ranges, respectively.

For the analysis of the electrical response of the OASSS, the top $3\pi/8$ arc segment dominates the resistance change, while the rest can be neglected in the analytic model. The mechanical analysis above, together with the relationship between the electrical response and the deformation of the constantan material, yields (details shown in the text in the Supporting Information)

$$\begin{aligned}\frac{\Delta R}{R_0} = \varepsilon_{\text{applied}}\Big\{&18\pi(1 + 2\nu_{\text{con}})(\overline{r}_0 - \overline{d} + \overline{w}/2)\\ &\times [\overline{L} + 8\sqrt{\sqrt{2} + 1}/(3\pi)][2\overline{d} - 2\overline{a}\\ &- (I_{zr}/I_{rr})(\overline{h}_{\text{PI}} + \overline{h}_{\text{con}} - 2\overline{b}) - \overline{w}]\Big\}\\ &/\{\overline{r}_0[3\pi(\overline{r}_0 - \overline{d} + \overline{w}/2) + \overline{r}_0\overline{w}(2\overline{L} + \pi)]\\ &\times [(\overline{EI}_{z,\text{arc}}/\overline{EI}_{z,\text{str}})\overline{L}^3 + 3\pi\overline{L}^2 + 24\overline{L} + 6\pi]\}\end{aligned} \quad (2)$$

For comparison, the OASSSs with the above seven sets of geometric parameters are fabricated and tested, with eight consecutive loading−unloading cycles applied for each OASSS.

https://doi.org/10.1021/acsnano.1c07645
ACS Nano 2022, 16, 541−553

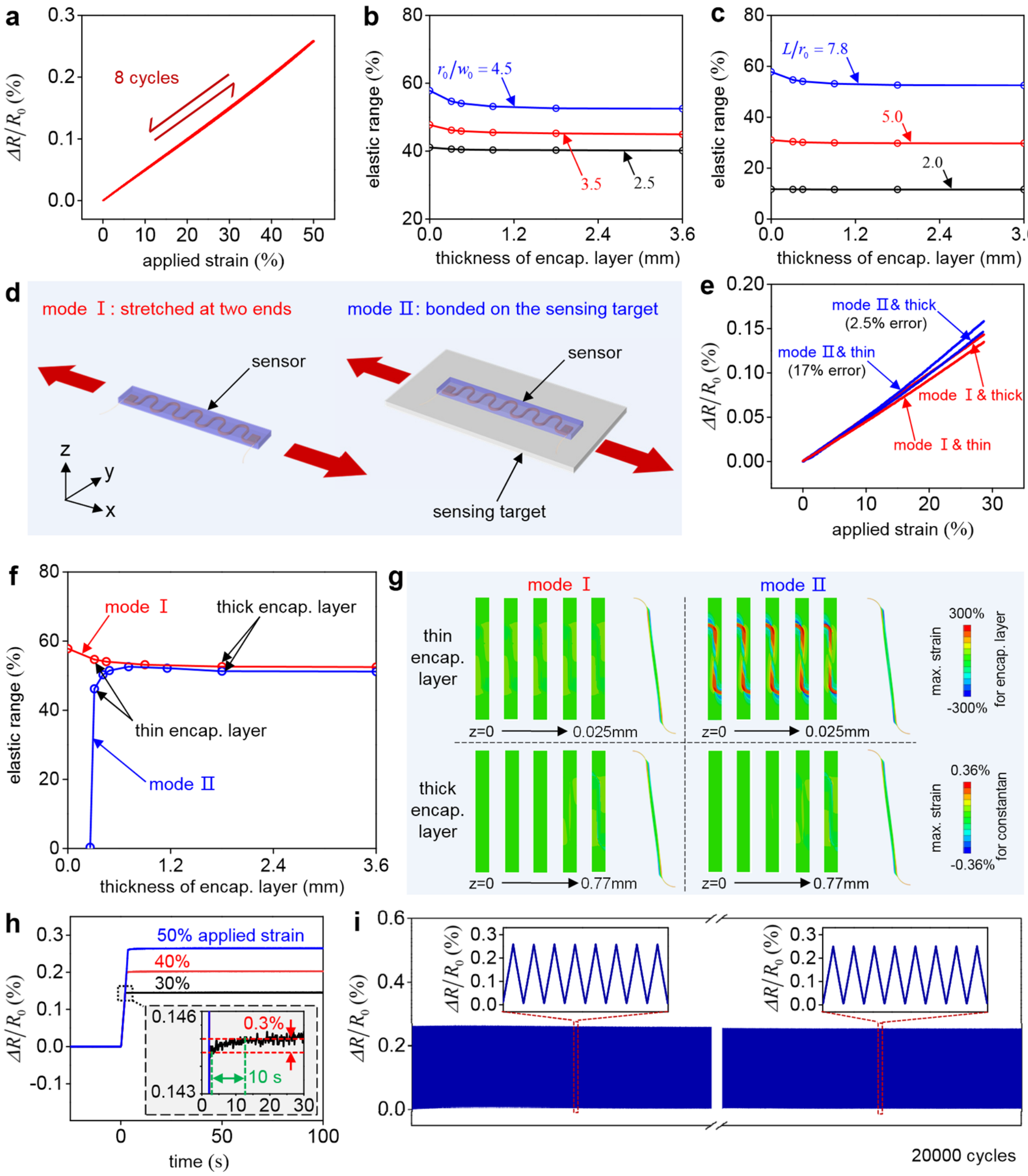

Figure 3. Mechanical and electrical characterization of the sensors with an encapsulation layer. (a) Relative resistance change of the sensor with and encapsulation layer *versus* the applied strain for eight consecutive loading−unloading cycles. (b) Effects of the thickness of the encapsulation layer on the elastic range under different dimensionless radii r_0/w_0 ($L/r_0 = 7.8$, $d/w_0 = 0.37$, and $w/w_0 = 0.12$). (c) Effects of the thickness of the encapsulation layer on the elastic range under different dimensionless lengths L/r_0 ($r_0/w_0 = 4.5$, $d/w_0 = 0.37$, and $w/w_0 = 0.12$). (d) Two modes of applying strain to the strain sensor. (e) Comparison of the electrical responses in the two modes with different thicknesses of the encapsulation layer. (f) Effect of the thickness of the encapsulation layer on the elastic range of the sensor in the two modes ($L/r_0 = 7.8$, $r_0/w_0 = 4.5$, $d/w_0 = 0.37$, and $w/w_0 = 0.12$). (g) Comparison of the strain distribution of the encapsulation layer and the OASSS in the two modes with different thicknesses of the encapsulation layer. (h) Relative resistance changes for a step strain (strain rate 14% s^{-1}) from 0% to 30%/40%/50%. Inset: close-up of the hysteresis of about 0.3%. (i) Relative resistance change under repeated loading and unloading of 50% strain for 20,000 cycles.

Figure 2g−i depicts the comparison of the analytic, experimental, and FEA (details shown in the Experimental Section) results incorporating the effects of $\overline{L}$, $\overline{r}_0$, and $\overline{d}$. They agree well with each other, which clearly shows that the electrical response is highly linearly proportional to the applied strain. The high linearity in a large sensing range could be explained as follows. In the present OASSS, the length of the straight segments is longer than the radius of the arc segments; thus, the applied strain is mainly contributed by the rotation of the straight segments. Even a small rotation much less than 1 (at B' in Figure 2c) is able to realize an applied strain as large as 100% (noting that the displacement caused by the rotation is along the stretching direction of the sensor). Owing to the small strain ($\varepsilon_{con,max}$) and the small rotation, all the constitutive and geometric relations of the OASSS are in the range of linearity according to the theory of solid mechanics,[48] which yields the linear relationship between the applied strain and the electrical response. Although the contact-resistance-free structures may have various forms, the OASSS is the best one that can be found at present to coordinate the high linearity and the high stretchability to a great extent. Moreover, experimental tests far beyond the theoretical elastic range have also been conducted for the above structures. As shown in Figure S10, the linearity and the repeatability hold well. Since the elastic limit of the constantan foil may be larger than 0.3% in practice, the theoretical elastic range allowing the maximum strain of 0.3% for the constantan foil is a safe estimation.

Mechanical and Electrical Characterization of Stretchable Strain Sensors with Encapsulation Layers. The complete stretchable sensor consists of the OASSS and the encapsulation layers as shown in Figure 1a and b. Figure 3a shows the experimental results of a stretchable sensor (initial resistance at zero strain = 838.7 Ω; detailed layouts shown in Figure S11a, the constantan foil in the straight segment is narrower than PI to expand the elastic range) with encapsulation layers for eight consecutive loading−unloading cycles. Here, in order to make the tensile test easier, the sensor is designed with 30 periods (overall width, 4.6 mm; overall length, 85 mm), although it could be shorter (such as overall length of 22 mm for seven periods, Figure S11b). Images of the sensor at 10%, 30%, and 50% applied strain are shown in Figure S12. The extremely high repeatability (δ_R = 1.58%) and linearity (R^2 from 0.99911 to 0.99964 for the 8 cycles) hold for the relationship between $\Delta R/R_0$ and the 0−50% applied strain, which is much better than the previously reported representative results.[5,23,29,30,49] As a comparison, a recent work[23] based on strain-mediated contact in anisotropically resistive structures exhibited a fine linearity (R^2 > 0.98), which may be enough in wearable applications but cannot satisfy the requirements of accurate measurement in aerospace and medical surgery. Besides, the repeatability error δ_R in many works based on the contact-resistance mechanism usually reaches ∼10%.[5,30] The high repeatability and linearity in this work are guaranteed because neither unstable contact resistance nor nonlinear constitutive and geometric behaviors occur during the sensing process. Unlike the curves of the relative resistance change *versus* the applied strain, the tensile stress−strain curves (Figure S13) do not exhibit high linearity, because of the hyperelasticity and viscoelasticity of the encapsulation material. However, the linearity of the electrical response is not affected since the resistance change only depends on the geometrical change of the OASSS (not involving the stress of the encapsulation material). If the applied strain of this sensor exceeds the elastic range of 50%, such as 100%, constantan undergoes plastic deformation and the sensor loses good repeatability (Figure S14). The GF, the ratio of the relative resistance change to the applied strain, is calculated as 0.0052. Such a GF value (not optimal) does not affect the high sensing performance of the sensor. The ideal resolution calculated by a recent theoretical study is about 0.0015% in the range of ε = [0.05%, 50%] (more details shown in Figure S15 and the text in the Supporting Information).[27] As shown in Figure 3a and Figure S16, the stretching tests verify that the strain sensor does have a high resolution to detect not only a large strain up to 50% but also an extremely small strain as low as 0.05%, which is much better than most previous results.[5,39,50] If the GF is 1 or 2 orders of magnitude smaller, an extremely high-precision instrument is required to detect such a small strain. Fortunately, the GF of the present sensor is enough to ensure the measurement by a conventional instrument or a portable circuit board. Mechanical analysis shows that the elastic range of the OASSS may be reduced by the constraints of the encapsulation layers (details shown in Figure S17 and the text in the Supporting Information). The effects of the thickness of the encapsulation layer are studied in Figure 3b and c. With the increase of the thickness, the elastic range decreases and approaches a stable value because excessively thick encapsulation does not provide more constraints. Figure 3b and c also shows the effects of $\overline{r}_0$ and $\overline{L}$ on the elastic range, which are beneficial for the optimization of the elastic range. Considering that the encapsulation materials used in practice are usually soft and thus have only a little effect on the elastic range, eq 1 can be used to estimate the dimensions of the sensors (details shown in the text in the Supporting Information). On this basis, the accurate elastic range should be verified by finite element analysis.

In a commonly used calibration test, the two ends of the sensor are fixed on the mechanical tensile equipment, while the middle segment is freestanding, as shown in the left subimage of Figure 3d (mode I). The relationship between the electrical response and the applied strain can be obtained subsequently. However, in many practical applications, the entire sensor is bonded on the sensing target, as depicted in the right subimage of Figure 3d (mode II). They share the strain distribution at the interface anywhere, of which the mechanical condition is different from the calibration test. The optimal design of the sensor needs to yield the same electrical response for both modes under the same applied strain such that the calibration result is universal for both application modes. The effects of the thickness of the encapsulation layer for both modes are studied by the experiments and FEA in Figure 3e−g. Figure 3e shows that the two modes give much different electric responses (17% relative error) for a thin encapsulation layer (thickness of 0.31 mm), while a thick encapsulation layer (thickness of 1.8 mm) yields almost the same electrical responses (2.5% relative error). Figure 3f compares the elastic range of the two modes. The elastic range of mode II sharply decreases for a small thickness of the encapsulation layer, while that of mode I gradually increases. However, both of them merge to a stable value with the increase of the thickness of the encapsulation layer. The key underlying mechanism can be understood by the investigation of the strain distribution (Figure 3g). For the same stretchable strain sensor, the FEA results show that the strain distributions in the encapsulation layer as well as the OASSS are almost the same for the two modes if the encapsulation layer is thick enough. For a thin encapsulation layer, the sensing target strongly constrains the deformation of the OASSS such that a very low elastic range is obtained for mode II, while the OASSS is almost freestanding such that a high elastic range is obtained for mode I. Therefore, the optimal strategy with thick encapsulation layers enables the universality of the calibration results. The consistency of the electrical responses in these two modes is proposed as an important indicator for stretchable strain sensors.

The dynamic performance is studied in Figure 3h. When 30% strain is applied at a strain rate of 14% s^{-1}, only 0.3% hysteresis occurs, which is much better than most previously reported strain sensors.[5,30] As a comparison, a graphene-based strain sensor[5] and a carbon nanotube strain sensor[30] both exhibited ∼3% dynamic error. As shown in Figure S18, the relative resistance changes of the sensor are almost the same at different strain rates of 2.9% s^{-1}, 8.6% s^{-1}, and 14.4% s^{-1}, which is consistent with the result in Figure 3h. Furthermore, the stability is also very important for practical applications of the stretchable strain sensors. As suggested in Figure 3i, the

https://doi.org/10.1021/acsnano.1c07645
ACS Nano 2022, 16, 541−553

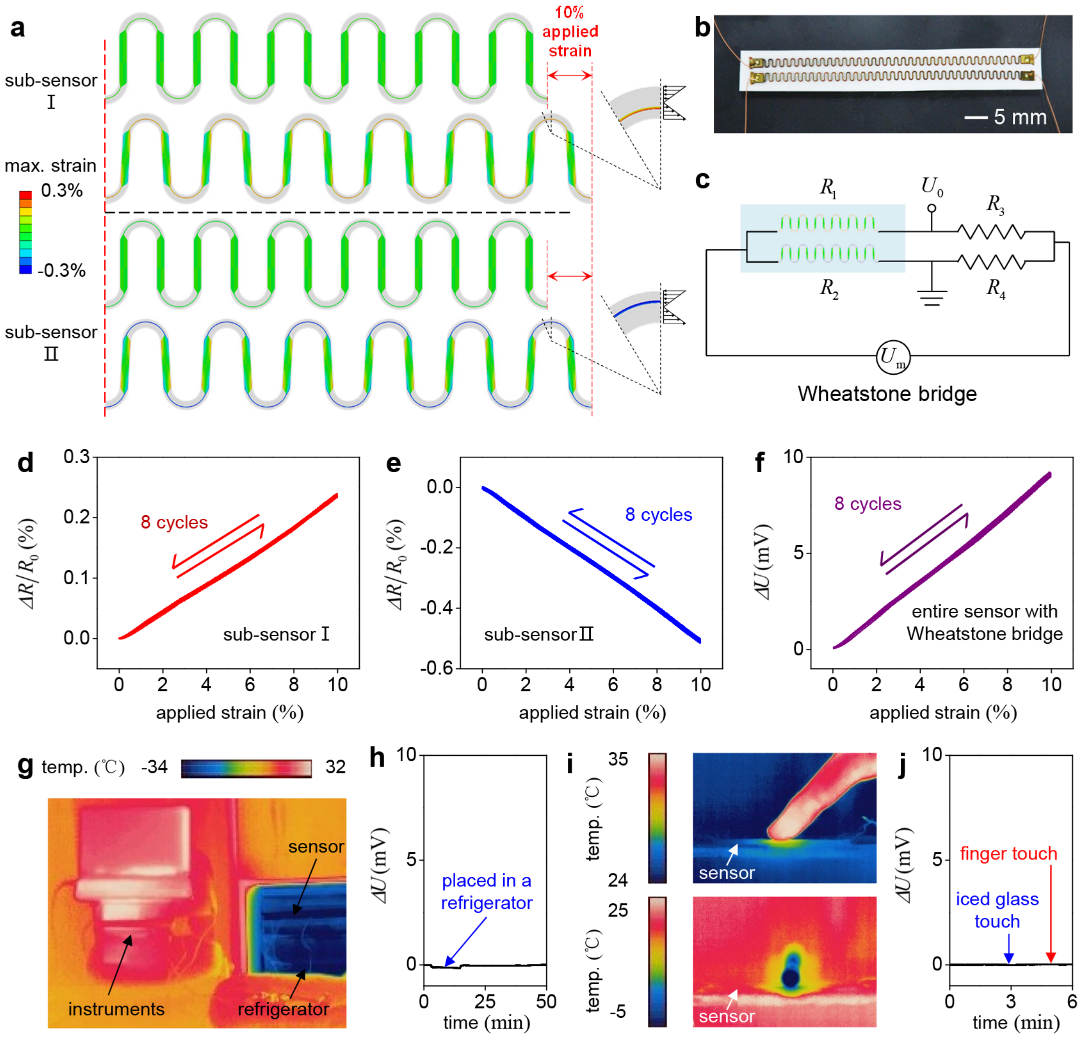

Figure 4. Design of temperature self-compensation. (a) FEA results of the two subsensors deformed by 10% applied strain: subsensor I, applied strain leads to a stretching strain of the constantan foil and an increase in resistance; subsensor II, applied strain leads to a compressive strain of the constantan foil and a decrease in resistance. (b) Image of an integrated strain sensor with temperature self-compensation. (c) Wheatstone bridge circuit for the measurement. (d and e) Relative resistance changes of subsensors I and II *versus* the applied strain for eight consecutive loading−unloading cycles. (f) Increment of the output voltage of the Wheatstone bridge *versus* the applied strain for eight consecutive loading−unloading cycles. (g) Infrared thermogram of the strain sensor with temperature self-compensation placed in a refrigerator. (h) Increment of the output voltage when the strain sensor with the temperature self-compensation was placed in a refrigerator. (i) Infrared thermograms of the strain sensor touched by a finger and an iced glass rod. (j) Increment of the output voltage when the strain sensor was touched by a finger or an iced glass.

performances, including sensing range (0−50%), repeatability, and linearity, hold during the 20,000 loading and unloading cycles, which is highly practical. Another sensor with a different layout shows the repeatability as high as 100,000 cycles under 25% applied strain (Figure S19). The high repeatability is guaranteed because neither unstable contact resistance nor plastic behavior occurs during the sensing process. In addition to the electrical responses in Figure 3i and Figure S19, the comparison of the micrographs before and after 5000 loading and unloading cycles shows that the constantan foil of the sensor is not found to be destroyed (Figure S20).

Design of Temperature Self-compensation. The effect of the temperatures of the environment and the sensing target on strain sensing is of importance for practical applications of the stretchable strain sensors. One way to reduce the influence of the temperature is to use sensing materials with low temperature coefficient of resistance such as constantan ($\sim 10^{-6}$ °C^{-1}, Figure S21a and b), while an additional approach is the design of temperature self-compensation. For this purpose, a design of temperature self-compensation is developed based on the special OASSS, which can be effective for a temperature range of tens of degree Celsius. As an extension of the basic design (Figure 1d), Figure 4a shows that the constantan foil is subjected to a stretching/compressive strain because it is located at the inside/outside of the central axis of the serpentine PI substrate. Therefore, the resistance changes of the two sensors are with opposite signs (the GFs for the applied strain $K_1 > 0$ and $K_2 < 0$), although they are subjected to the same applied strain. On the other hand, the temperature variation of the environment yields the same resistance change for the two sensors (the temperature coefficient of resistance $\alpha > 0$). The sensors of the two types can be integrated into one sensor (Figure 4b), and the Wheatstone bridge circuit can be adopted for the measurement

https://doi.org/10.1021/acsnano.1c07645
ACS Nano 2022, 16, 541−553

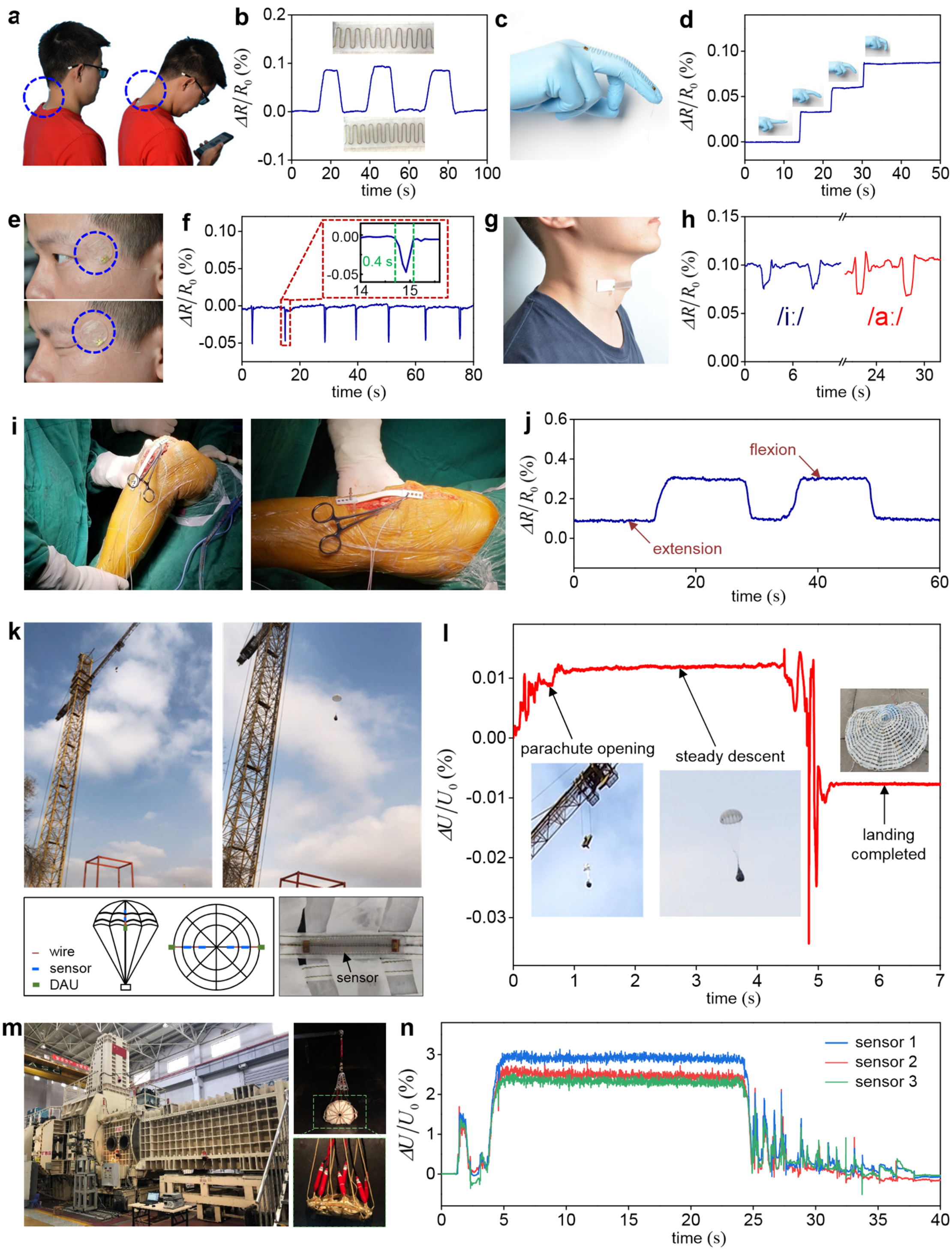

Figure 5. Representative applications to monitoring human activities, total knee arthroplasty, and aerospace equipment. (a) Image of the sensor attached to the back of the neck. (b) Signals of motions of the neck. (c) Image of the sensor integrated to the finger of a smart glove. (d) Signals of the bending of a finger. (e) Image of the sensor attached near the corner of the eye to monitor the motion of blinking. (f) Signals showing the rapid and tiny muscular movement caused by blinking. Insets: close-up of one blinking. (g) Image of the sensor attached to a boy's throat for phonation recognition. (h) Signals of phonation when the boy spoke /i:/ and /a:/. (i) Image of the extension and flexion of the knee. (j) Signals of the deformation of the ligament when the knee was extended/flexed. (k) Images of the drop test from a 110 m high tower and the layout of the sensing system. (l) Signal of the deformation of the radial belt during the drop test. (m) Images of the wind tunnel (left) and the parachute integrated with the strain sensors placed in the wind tunnel (right). (n) Signals of the deformation of the parachute ropes during the wind tunnel test.

(Figure 4c). Their resistances become $R_1 = (1 + K_1\varepsilon_{\text{applied}})(1 + \alpha\Delta T)\,R_{10}$ and $R_2 = (1 + K_2\varepsilon_{\text{applied}})(1 + \alpha\Delta T)R_{20}$, respectively, if the entire sensor is subjected to an applied strain $\varepsilon_{\text{applied}}$ and a temperature variation ΔT. Here, R_{10} andR_{20} are the resistances at the initial regime. The increment of the output voltage ΔU_m can be obtained as

$$\Delta U_{\mathrm{m}} = \frac{K_1\left(\cancel{1+\alpha\Delta T}\right)R_{10} - K_2\left(\cancel{1+\alpha\Delta T}\right)R_{20}}{2\left[\left(\cancel{1+\alpha\Delta T}\right)R_{10} + \left(\cancel{1+\alpha\Delta T}\right)R_{20}\right]}U_0\varepsilon_{\mathrm{applied}}$$

$$= \frac{K_1R_{10} - K_2R_{20}}{2\left(R_{10}+R_{20}\right)}U_0\varepsilon_{\mathrm{applied}} \quad (3)$$

Here, U_0 is the input voltage of the Wheatstone bridge; $R_3 = R_4$ is applied in the derivation of eq 3 (details shown in the text in the Supporting Information). With the present design and Wheatstone bridge, the effect of the temperature is eliminated while the function of strain sensing holds.

The sensor with temperature self-compensation is fabricated and tested to validate the design. The stretching test is applied to the sensor for eight consecutive loading–unloading cycles. The experimental results show that the high repeatability and linearity hold for the two subsensors (Figure 4d and e) and the entire sensor with the Wheatstone bridge (Figure 4f). The GFs of the two subsensors appear with opposite signs as predicted. In order to validate the function of temperature self-compensation, the sensor is placed in a refrigerator during the test (Figure 4g and Figure S22a). The output voltage is almost unchanged while the sensor undergoes a temperature variation of as high as 60 °C (Figure 4h). The calculated temperature coefficient of voltage is as low as $(\Delta U_{\mathrm{m}}/U_0)/\Delta T = 5 \times 10^{-7}$ °C^{-1}. Furthermore, a portion of the sensor is touched by an iced glass and a finger with a temperature difference of 30 and 11 °C, respectively (Figure 4i and j and Figure S22b and c). The output voltage is also unchanged because the sensor is narrow and long, and the temperature change is applied to the two subsensors with the same level. More results about the relative change in output voltage *versus* temperature variation (relative to 25 °C) are shown in Figure S23 and the text in the Supporting Information.

Representative Applications to Monitoring Human Activities, Medical Surgery, and Aerospace Equipment. The high performance of the present sensor exhibits great potential in applications related to human bodies, including motion detection, gesture recognition, surgical assistance, postoperative rehabilitation, human–machine interaction, *etc.* Figure 5a–d and Figure S24a and b show the ability of the stretchable strain sensor to detect large motions of the human body. Since the number of people with cervical spondylopathy has been increasing quickly in recent years because of the popularization of smart phones, a wearable device based on the present sensor (Figure 5a and b), capable of monitoring the real-time motions of the neck and reminding, is of great significance for protecting people against diseases. Figure 5c and d and Figure S24a and b illustrate a glove integrating the present sensors, which can detect the bending of the finger and the wrist. A smart glove integrated with the present sensors may be used for facilitating fine-motion control in robotics, providing a method of automatic understanding in the deaf community, monitoring the finger motions of patients in a minimally conscious or vegetative state, *etc.* Subtle human motions, such as phonation, blinking, and respiration, could also be instantly and accurately detected by the present sensor. As a demonstration, the strain sensor was used to monitor the motion of blinking (Figure 5e). To achieve ergonomics in wiring, the two electrodes are preferably at the same end. Such a connection mode can be achieved on the basis of the original design. As shown in Figure S25, two identical OASSSs are electrically connected in series at the right end, and thus, the two electrodes are only needed to be set at the left end. The subtle movement of the facial muscle located at the corner of a human eye could be accurately captured (Figure 5f). The sensor was also attached to the skin of a boy's throat for phonation recognition (Figure 5g). The phonations of /i:/ and /a:/ were distinguished by the different waveforms of the output resistance change (Figure 5h). Respiration is an important physiological signal that can be monitored by the present sensor. Figure S24c and d shows discriminable and steady breathing waveforms and frequency (10 min^{-1}), indicating potential applications for monitoring sudden infant death syndrome and sleep apnea in adults.

Moreover, the stretchable strain sensor has the potential to be applied in orthopedic surgical scenarios where soft tissue stretching needs to be monitored. For example, in total knee arthroplasty, the intraoperative patellar tendon strain during extension and flexion of the knee can be measured with the strain sensor, providing real-time information to surgeons whether the length and tension of the patella tendon are appropriate, which could help optimizing the postoperative function of the knee joint. As a demonstration, the present sensor is applied in a clinical trial. The sensor is fabricated and calibrated on a tensile testing machine (Figure S26a). An additional test on a glass tube with 1.5 cm diameter verifies that the bending deformation can hardly affect the stretching sensing (Figure S26b), which ensures the accuracy of the strain measurement during bending of the knee. After the ethylene epoxide disinfection for 16 h, the two ends of the sensor are fixed to the patella and tibial tubercle, respectively, in the extension regime of the knee. When installing the stretchable strain sensor onto the patella tendon, practical operation cannot ensure that the installing regime of the sensor is strain-free; thus, high linearity is required such that the measured strain will be insensitive to the prestrain of the sensor. Figure 5i shows the extension and flexion of the knee when the real-time strain variation is accurately captured (Figure 5j and Figure S26c and d). Based on the present sensor, a professional piece of equipment may be developed for a more convenient surgical operation.

Furthermore, owing to its high performance including sensing range, repeatability, linearity, temperature insensitivity, and flexibility, the present sensor has the potential to be applied in aerospace equipment where a large number of key components with flexible and stretchable characteristics urgently need sensing under extremely high temperature change. For example, the parachute is mainly made of soft fabric, which is widely used for deceleration and stabilization for spacecraft landing. By measuring the deformation of the parachute ropes, radial belts and zonal belts, the degree of deformation heterogeneity and the dangerous position can be obtained, and whether there is slip at the insertion position can be deduced, so as to help optimize the parachute design. The present sensor has been applied in the ground tests of the scaled parachute of Tianwen-1 (China's first Mars exploration mission). Different from health monitoring, which sometimes only needs a rough curve, the ground tests of Tianwen-1 require a high accuracy to help optimize the parachute design; thus, a high repeatability is essential to ensure that the calibration relationship is consistent with the initial calibration time. Figure 5k shows the drop test from a 110 m high tower and the layout of the sensing system that is composed of the sensors, wires, and data acquisition units (DAUs, Figure S27). The corresponding real-time voltage variation (only part of the

https://doi.org/10.1021/acsnano.1c07645
ACS Nano 2022, 16, 541−553

data is shown) is accurately captured, and the three stages can be clearly distinguished (Figure 5l). After the preliminary verification of the drop test, the strain sensors further provide real-time strain monitoring of the parachute ropes in wind tunnel tests with Mach numbers from 1.5 to 3 under the extremely high temperature change, the impact of high-speed air flow, and the sharp shaking of the parachute ropes (Figure 5m). The voltage curves (only part of the data is shown) reflect the lack of consistency in the early parachute (Figure 5n). In future exploration missions, the present sensor may be integrated into the parachute and land on an alien planet to feed back the deformation of the parachute in real time. Another example is the strain measurement of a high-altitude balloon (a kind of unpowered aerostat flying in the stratosphere) to avoid the membrane strain of the film (thin and soft) from reaching the limit, as the strain limit of the film is one of the important factors affecting the flight performance and service life of a high-altitude balloon. As shown in Figure S28, the ground test has preliminarily verified the feasibility of the present sensor when applied to strain monitoring of the high-altitude balloon. The variation trend of the measured strain is highly consistent with that of the air pressure given by an inflator.

CONCLUSIONS

In summary, a design for stretchable strain sensors based on contact-resistance-free structures is proposed. The stretchable strain sensor consists of an OASSS, with the mechanism of the SBST to accomplish a large sensing range of ∼50%, and two encapsulation layers. Experimental fabrication, including spin coating, lithography, laser cutting, *etc.*, mechanical and electrical tests, and FEA are carried out. Collective results show that a high elastic range can be achieved by using a large radius of the arc segment, small width of the PI substrate, large length of the straight segment, and large thickness of the encapsulation layers. Neither unstable contact resistance nor nonlinear constitutive and geometric behaviors occur during the sensing process, which is the key difference from the strategy of the contact-resistance mechanism. Therefore, high repeatability (δ_R = 1.58%) and linearity (R^2 > 0.999) are guaranteed. Temperature self-compensation is accomplished (temperature coefficient of voltage = 5×10^{-7} °C^{-1}) by a design taking advantage of the special OASSS and the Wheatstone bridge circuit. We show that the stretchable strain sensor can be applied not only to monitoring human activities, including real-time motions of the neck, fingers, wink, phonation, and breathing, but also to medical surgery such as total knee arthroplasty, and even to aerospace equipment such as the parachute (the ground tests of China's first Mars exploration mission Tianwen-1) and the high-altitude balloon. Although some stable contact structures may be developed in the future, directly avoiding the employment of the contact-resistance mechanism is always an effective way to achieve high repeatability and linearity at this stage and in the future. The design idea of employing contact-resistance-free structures and the OASSS can be extended by using various functional materials.

EXPERIMENTAL SECTION

Fabrication Process of the Strain Sensors. As shown in Figure S2, the fabrication processes of the strain sensors were the following. Step 1: A PI layer was spin-coated (2,000 rpm for 60 s) on a 5-μm-thick commercial constantan foil (Hanzhong Jingce, China) and cured at 250 °C for 4 h. The process was repeated 8 times to thicken the PI layer to 50 μm. A layer of a 200-μm-thick PI film was laminated on the 50-μm-thick PI layer by a resin adhesive. Step 2: The constantan layer was patterned to the off-axis serpentine structure by a standard photolithography process (including coating photoresist, prebaking, UV exposure, development, corrosion of ferric chloride solution, and removal of photoresist). Step 3: Two copper wires were soldered to both ends of the serpentine structure as the electrodes to connect to the outside circuit. Step 4: A layer of a 10-μm-thick PI film was laminated on the constantan layer by a resin adhesive to constitute a PI/constantan/PI sandwich structure. Step 5: The sandwich structure was patterned to get the OASSS by a UV picosecond laser (DL566PU, DCT, China). Steps 6 and 7: The patterned OASSS was encapsulated with a 1.8-mm-thick encapsulation layer (Ecoflex 00-30, Smooth-On, USA) by a two-stage lamination, *i.e.*, laminating the structure on a fabricated Ecoflex film (step 6) and coating another layer of a 1:1 liquid mixture of Ecoflex above the structure followed by curing (step 7). If plasma etching is used instead of wet etching and laser cutting in the fabrication process, the manufacturing accuracy will be significantly improved, and thus, the size can be greatly reduced by 1 order of magnitude.

Characterization of the Strain Sensors. Static, dynamic, and cyclic stretching tests of the stretchable strain sensors were carried out by two programmable tensile testing machines (ZQ-990A, ZHIQU, China and 5848 Microtester, Instron, USA), as shown in Figure S5. The resistance and voltage signals of the sensors were measured by a digital multimeter (34461A, Keysight, USA). The strain sensor with temperature self-compensation was powered by a programmable DC power (DP831A, RIGOL, China).

Finite Element Analyses of Deformation. The FEA was performed employing the commercial software ABAQUS (SIMULIA, France) to verify the mechanical model of the OASSS. A half period of the OASSS was used for the FEA model, with the boundary conditions of zero displacement imposed in the x direction at one end cross section and a displacement load of $2r_0\varepsilon_{\text{applied}}$ in the same direction at another end cross section. The material parameters of Ecoflex, which was regarded as a hyperelastic material described by the Mooney−Rivlin model, were C_{10} = 0.00805369 MPa, C_{01} = 0.00201342 MPa, and D_1 = 2 MPa^{-1}, respectively. PI (elastic modulus = 2.5 GPa and Poisson's ratio = 0.34) and constantan (elastic modulus = 163 GPa and Poisson's ratio = 0.33) were both regarded as linear elastic materials. The hexahedron element C3D8RH was utilized for Ecoflex and the hexahedron element C3D8R for PI and constantan. As shown in Figure S9a, the deformation result of the FEA agrees well with that of the experiment.

Finite Element Analyses of the Change in Resistance. The model of resistance variation of the OASSS was solved by FEA with the commercial software COMSOL. The steady-state research was carried out by choosing two physical fields, *i.e.*, "electric currents" and "solid mechanics". The mechanical boundary conditions were the same as those in ABAQUS, while the electrical boundary conditions were set such that one end of the OASSS was grounded and another acted as a terminal to give a current of 1 A. The elastic moduli and Poisson's ratios were the same as those outlined in the previous section, and the conductivity of constantan was set to 2.0833×10^6 S/m. The resistance of the constantan foil was obtained by dividing the electric potential in the terminal (Figure S9b) by the current of 1 A.

Additional Experimental Details. The experiments involving human volunteers were approved by the Institutional Review Board at Institute of Mechanics, Chinese Academy of Sciences (Approval No. 2021003), wherein the volunteers took part following informed consent.

ASSOCIATED CONTENT

Supporting Information

The Supporting Information is available free of charge at https://pubs.acs.org/doi/10.1021/acsnano.1c07645.

Experimental details and theoretical analyses of the stretchable strain sensors (PDF)

https://doi.org/10.1021/acsnano.1c07645
ACS Nano 2022, 16, 541−553

AUTHOR INFORMATION

Corresponding Author

Yewang Su – *State Key Laboratory of Nonlinear Mechanics, Institute of Mechanics, Chinese Academy of Sciences, Beijing 100190, China; School of Engineering Science, University of Chinese Academy of Sciences, Beijing 100049, China; State Key Laboratory of Structural Analysis for Industrial Equipment, Department of Engineering Mechanics, Dalian University of Technology, Dalian 116024, China;* orcid.org/0000-0002-5961-0490; Email: yewangsu@imech.ac.cn

Authors

Shuang Li – *State Key Laboratory of Nonlinear Mechanics, Institute of Mechanics, Chinese Academy of Sciences, Beijing 100190, China; School of Engineering Science, University of Chinese Academy of Sciences, Beijing 100049, China*

Guodong Liu – *State Key Laboratory of Nonlinear Mechanics, Institute of Mechanics, Chinese Academy of Sciences, Beijing 100190, China; School of Engineering Science, University of Chinese Academy of Sciences, Beijing 100049, China*

Rui Li – *State Key Laboratory of Structural Analysis for Industrial Equipment, Department of Engineering Mechanics, and International Research Center for Computational Mechanics, Dalian University of Technology, Dalian 116024, China*

Qinlan Li – *State Key Laboratory of Nonlinear Mechanics, Institute of Mechanics, Chinese Academy of Sciences, Beijing 100190, China; School of Engineering Science, University of Chinese Academy of Sciences, Beijing 100049, China*

Yang Zhao – *State Key Laboratory of Nonlinear Mechanics, Institute of Mechanics, Chinese Academy of Sciences, Beijing 100190, China; School of Engineering Science, University of Chinese Academy of Sciences, Beijing 100049, China*

Mingqi Huang – *State Key Laboratory of Structural Analysis for Industrial Equipment, Department of Engineering Mechanics, and International Research Center for Computational Mechanics, Dalian University of Technology, Dalian 116024, China*

Maoyi Zhang – *State Key Laboratory of Nonlinear Mechanics, Institute of Mechanics, Chinese Academy of Sciences, Beijing 100190, China; School of Engineering Science, University of Chinese Academy of Sciences, Beijing 100049, China*

Shizhen Yin – *State Key Laboratory of Nonlinear Mechanics, Institute of Mechanics, Chinese Academy of Sciences, Beijing 100190, China; School of Engineering Science, University of Chinese Academy of Sciences, Beijing 100049, China*

Yixin Zhou – *Department of Orthopaedic Surgery, Beijing Jishuitan Hospital, Fourth Clinical College of Peking University, Beijing 100035, China*

Hao Tang – *Department of Orthopaedic Surgery, Beijing Jishuitan Hospital, Fourth Clinical College of Peking University, Beijing 100035, China*

Liwu Wang – *Beijing Institute of Space Mechanics & Electricity, Beijing 100094, China*

Guanhui Fang – *Beijing Institute of Space Mechanics & Electricity, Beijing 100094, China*

Complete contact information is available at: https://pubs.acs.org/10.1021/acsnano.1c07645

Author Contributions

S.L. and Y.S. conceived the concept. S.L., G.L., R.L., Q.L., Y.Z., M.H., M.Z., S.Y., Y.Z., H.T., L.W., G.F., and Y.S. conducted the theoretical derivation, experimental fabrication, and performance test and discussed all the data. S.L. and Y.S. prepared the manuscript. Y.S. supervised the project.

Notes

The authors declare no competing financial interest.

ACKNOWLEDGMENTS

Y.S. gratefully acknowledges the support from the National Natural Science Foundation of China (grants 11772331 and 12172359), Beijing Municipal Science and Technology Commission (Z191100002019010), Beijing Municipal Natural Science Foundation (No. 2202066), Key Research Program of Frontier Sciences of the Chinese Academy of Sciences (ZDBS-LY-JSC014), CAS Interdisciplinary Innovation Team (JCTD-2020-03), Strategic Priority Research Program of the Chinese Academy of Sciences (No. XDB22040501), Beijing Institute of Space Mechanics & Electricity, and the State Key Laboratory of Structural Analysis for Industrial Equipment, Dalian University of Technology (No. GZ19102). R.L. gratefully acknowledges the support from the National Natural Science Foundation of China (grants 12022209 and 11972103), Liaoning Revitalization Talents Program (grant XLYC1807126), and the Fundamental Research Funds for the Central Universities (grant DUT21LAB124).

REFERENCES

(1) Bai, H. D.; Li, S.; Barreiros, J.; Tu, Y. Q.; Pollock, C. R.; Shepherd, R. F. Stretchable Distributed Fiber-Optic Sensors. *Science* **2020**, *370*, 848−852.

(2) Mickle, A. D.; Won, S. M.; Noh, K. N.; Yoon, J.; Meacham, K. W.; Xue, Y. G.; McIlvried, L. A.; Copits, B. A.; Samineni, V. K.; Crawford, K. E.; Kim, D. H.; Srivastava, P.; Kim, B. H.; Min, S.; Shiuan, Y.; Yun, Y.; Payne, M. A.; Zhang, J. P.; Jang, H.; Li, Y. H.; et al. A Wireless Closed-Loop System for Optogenetic Peripheral Neuromodulation. *Nature* **2019**, *565*, 361−365.

(3) Niu, S. M.; Matsuhisa, N.; Beker, L.; Li, J. X.; Wang, S. H.; Wang, J. C.; Jiang, Y. W.; Yan, X. Z.; Yun, Y. J.; Burnetts, W.; Poon, A. S. Y.; Tok, J. B. H.; Chen, X. D.; Bao, Z. N. A Wireless Body Area Sensor Network Based on Stretchable Passive Tags. *Nat. Electron.* **2019**, *2*, 361−368.

(4) Zhou, Z. H.; Chen, K.; Li, X. S.; Zhang, S. L.; Wu, Y. F.; Zhou, Y. H.; Meng, K. Y.; Sun, C. C.; He, Q.; Fan, W. J.; Fan, E. D.; Lin, Z. W.; Tan, X. L.; Deng, W. L.; Yang, J.; Chen, J. Sign-to-Speech Translation Using Machine-Learning-Assisted Stretchable Sensor Arrays. *Nat. Electron.* **2020**, *3*, 571−578.

(5) Cheng, Y.; Wang, R.; Sun, J.; Gao, L. A Stretchable and Highly Sensitive Graphene-Based Fiber for Sensing Tensile Strain, Bending, and Torsion. *Adv. Mater.* **2015**, *27*, 7365−7371.

(6) Liu, H.; Zhao, H. Y.; Li, S.; Hu, J. Q.; Zheng, X. R.; Li, R.; Chen, Y. L.; Su, Y. W. Adhesion-Free Thin-Film-Like Curvature Sensors Integrated on Flexible and Wearable Electronics for Monitoring Bending of Joints and Various Body Gestures. *Adv. Mater. Technol.* **2019**, *4*, 1800327.

(7) Bai, N. N.; Wang, L.; Wang, Q.; Deng, J.; Wang, Y.; Lu, P.; Huang, J.; Li, G.; Zhang, Y.; Yang, J. L.; Xie, K. W.; Zhao, X. H.; Guo, C. F. Graded Intrafillable Architecture-Based Iontronic Pressure Sensor with Ultra-Broad-Range High Sensitivity. *Nat. Commun.* **2020**, *11*, 209.

(8) Mannsfeld, S. C. B.; Tee, B. C. K.; Stoltenberg, R. M.; Chen, C. V. H. H.; Barman, S.; Muir, B. V. O.; Sokolov, A. N.; Reese, C.; Bao, Z. N. Highly Sensitive Flexible Pressure Sensors with Microstructured Rubber Dielectric Layers. *Nat. Mater.* **2010**, *9*, 859−864.

(9) Matsuhisa, N.; Kaltenbrunner, M.; Yokota, T.; Jinno, H.; Kuribara, K.; Sekitani, T.; Someya, T. Printable Elastic Conductors with a High Conductivity for Electronic Textile Applications. *Nat. Commun.* **2015**, *6*, 7461.

(10) Zhang, F.; Zang, Y.; Huang, D.; Di, C.-a.; Zhu, D. Flexible and Self-Powered Temperature−Pressure Dual-Parameter Sensors Using Microstructure-Frame-Supported Organic Thermoelectric Materials. *Nat. Commun.* **2015**, *6*, 8356.

(11) Pang, C.; Koo, J. H.; Nguyen, A.; Caves, J. M.; Kim, M. G.; Chortos, A.; Kim, K.; Wang, P. J.; Tok, J. B.; Bao, Z. Highly Skin-Conformal Microhairy Sensor for Pulse Signal Amplification. *Adv. Mater.* **2015**, *27*, 634−640.

(12) Khan, Y.; Han, D.; Pierre, A.; Ting, J.; Wang, X.; Lochner, C. M.; Bovo, G.; Yaacobi-Gross, N.; Newsome, C.; Wilson, R.; Arias, A. C. A Flexible Organic Reflectance Oximeter Array. *Proc. Natl. Acad. Sci. U. S. A.* **2018**, *115*, E11015−E11024.

(13) Schwartz, G.; Tee, B. C.; Mei, J.; Appleton, A. L.; Kim, D. H.; Wang, H.; Bao, Z. Flexible Polymer Transistors with High Pressure Sensitivity for Application in Electronic Skin and Health Monitoring. *Nat. Commun.* **2013**, *4*, 1859.

(14) Hu, H. J.; Zhu, X.; Wang, C. H.; Zhang, L.; Li, X. S.; Lee, S.; Huang, Z. L.; Chen, R. M.; Chen, Z. Y.; Wang, C. F.; Gu, Y.; Chen, Y. M.; Lei, Y. S.; Zhang, T. J.; Kim, N.; Guo, Y. X.; Teng, Y.; Zhou, W. B.; Li, Y.; Nomoto, A.; et al. Stretchable Ultrasonic Transducer Arrays for Three-Dimensional Imaging on Complex Surfaces. *Sci. Adv.* **2018**, *4*, eaar3979.

(15) Lee, J. S.; Oh, J.; Jun, J.; Jang, J. Wireless Hydrogen Smart Sensor Based on Pt/Graphene-Immobilized Radio-Frequency Identification Tag. *ACS Nano* **2015**, *9*, 7783−7790.

(16) Floreano, D.; Pericet-Camara, R.; Viollet, S.; Ruffier, F.; Bruckner, A.; Leitel, R.; Buss, W.; Menouni, M.; Expert, F.; Juston, R.; Dobrzynski, M. K.; L'Eplattenier, G.; Recktenwald, F.; Mallot, H. A.; Franceschini, N. Miniature Curved Artificial Compound Eyes. *Proc. Natl. Acad. Sci. U. S. A.* **2013**, *110*, 9267−9272.

(17) Jung, I. W.; Xiao, J. L.; Malyarchuk, V.; Lu, C. F.; Li, M.; Liu, Z. J.; Yoon, J.; Huang, Y. G.; Rogers, J. A. Dynamically Tunable Hemispherical Electronic Eye Camera System with Adjustable Zoom Capability. *Proc. Natl. Acad. Sci. U. S. A.* **2011**, *108*, 1788−1793.

(18) Amjadi, M.; Pichitpajongkit, A.; Lee, S.; Ryu, S.; Park, I. Highly Stretchable and Sensitive Strain Sensor Based on Silver Nanowire-Elastomer Nanocomposite. *ACS Nano* **2014**, *8*, 5154−5163.

(19) Rogers, J. A.; Someya, T.; Huang, Y. G. Materials and Mechanics for Stretchable Electronics. *Science* **2010**, *327*, 1603−1607.

(20) Sekitani, T.; Nakajima, H.; Maeda, H.; Fukushima, T.; Aida, T.; Hata, K.; Someya, T. Stretchable Active-Matrix Organic Light-Emitting Diode Display Using Printable Elastic Conductors. *Nat. Mater.* **2009**, *8*, 494−499.

(21) Zhang, L. J.; Jiang, X. X.; Jiang, W.; Li, S.; Chi, Y. X.; Liu, H.; Zhang, M. Y.; Li, J. Y.; Fang, M.; Pan, B.; Chen, Y. L.; Shen, C. N.; Guo, X.; Li, R.; Guo, L.; Su, Y. W. Infrared Skin-Like Active Stretchable Electronics Based on Organic-Inorganic Composite Structures for Promotion of Cutaneous Wound Healing. *Adv. Mater. Technol.* **2019**, *4*, 1900150.

(22) Zhang, M. Y.; Liu, H.; Cao, P.; Chen, B.; Hu, J. Q.; Chen, Y. L.; Pan, B.; Fan, J. A.; Li, R.; Zhang, L. J.; Su, Y. W. Strain-Limiting Substrates Based on Nonbuckling, Prestrain-Free Mechanics for Robust Stretchable Electronics. *J. Appl. Mech.-Trans. ASME* **2017**, *84*, 121010.

(23) Araromi, O. A.; Graule, M. A.; Dorsey, K. L.; Castellanos, S.; Foster, J. R.; Hsu, W. H.; Passy, A. E.; Vlassak, J. J.; Weaver, J. C.; Walsh, C. J.; Wood, R. J. Ultra-Sensitive and Resilient Compliant Strain Gauges for Soft Machines. *Nature* **2020**, *587*, 219−224.

(24) Cohen, D. J.; Mitra, D.; Peterson, K.; Maharbiz, M. M. A Highly Elastic, Capacitive Strain Gauge Based on Percolating Nanotube Networks. *Nano Lett.* **2012**, *12*, 1821−1825.

(25) Zhou, J.; Gu, Y. D.; Fei, P.; Mai, W. J.; Gao, Y. F.; Yang, R. S.; Bao, G.; Wang, Z. L. Flexible Piezotronic Strain Sensor. *Nano Lett.* **2008**, *8*, 3035−3040.

(26) Figliola, R. S.; Beasley, D. E. *Theory and Design for Mechanical Measurements*; Wiley: Hoboken, NJ, 2011.

(27) Li, S.; Liu, G. D.; Wang, L. W.; Fang, G. H.; Su, Y. W. Overlarge Gauge Factor Yields a Large Measuring Error for Resistive-Type Stretchable Strain Sensors. *Adv. Electron. Mater.* **2020**, *6*, 2000618.

(28) Li, S.; Zhang, Y.; Wang, Y.; Xia, K.; Yin, Z.; Wang, H.; Zhang, M.; Liang, X.; Lu, H.; Zhu, M.; Wang, H.; Shen, X.; Zhang, Y. Physical Sensors for Skin-Inspired Electronics. *InfoMat* **2020**, *2*, 184−211.

(29) Lipomi, D. J.; Vosgueritchian, M.; Tee, B. C.; Hellstrom, S. L.; Lee, J. A.; Fox, C. H.; Bao, Z. Skin-Like Pressure and Strain Sensors Based on Transparent Elastic Films of Carbon Nanotubes. *Nat. Nanotechnol.* **2011**, *6*, 788−792.

(30) Yamada, T.; Hayamizu, Y.; Yamamoto, Y.; Yomogida, Y.; Izadi-Najafabadi, A.; Futaba, D. N.; Hata, K. A Stretchable Carbon Nanotube Strain Sensor for Human-Motion Detection. *Nat. Nanotechnol.* **2011**, *6*, 296−301.

(31) Ryu, S.; Lee, P.; Chou, J. B.; Xu, R.; Zhao, R.; Hart, A. J.; Kim, S. G. Extremely Elastic Wearable Carbon Nanotube Fiber Strain Sensor for Monitoring of Human Motion. *ACS Nano* **2015**, *9*, 5929−5936.

(32) Liu, Z. F.; Fang, S.; Moura, F. A.; Ding, J. N.; Jiang, N.; Di, J.; Zhang, M.; Lepro, X.; Galvao, D. S.; Haines, C. S.; Yuan, N. Y.; Yin, S. G.; Lee, D. W.; Wang, R.; Wang, H. Y.; Lv, W.; Dong, C.; Zhang, R. C.; Chen, M. J.; Yin, Q.; et al. Hierarchically Buckled Sheath-Core Fibers for Superelastic Electronics, Sensors, and Muscles. *Science* **2015**, *349*, 400−404.

(33) Li, L.; Xiang, H.; Xiong, Y.; Zhao, H.; Bai, Y.; Wang, S.; Sun, F.; Hao, M.; Liu, L.; Li, T.; Peng, Z.; Xu, J.; Zhang, T. Ultrastretchable Fiber Sensor with High Sensitivity in Whole Workable Range for Wearable Electronics and Implantable Medicine. *Adv. Sci.* **2018**, *5*, 1800558.

(34) Boland, C. S.; Khan, U.; Backes, C.; O'Neill, A.; McCauley, J.; Duane, S.; Shanker, R.; Liu, Y.; Jurewicz, I.; Dalton, A. B.; Coleman, J. N. Sensitive, High-Strain, High-Rate Bodily Motion Sensors Based on Graphene-Rubber Composites. *ACS Nano* **2014**, *8*, 8819−8830.

(35) Yan, C.; Wang, J.; Kang, W.; Cui, M.; Wang, X.; Foo, C. Y.; Chee, K. J.; Lee, P. S. Highly Stretchable Piezoresistive Graphene-Nanocellulose Nanopaper for Strain Sensors. *Adv. Mater.* **2014**, *26*, 2022−2027.

(36) Tang, Y.; Zhao, Z.; Hu, H.; Liu, Y.; Wang, X.; Zhou, S.; Qiu, J. Highly Stretchable and Ultrasensitive Strain Sensor Based on Reduced Graphene Oxide Microtubes-Elastomer Composite. *ACS Appl. Mater. Interfaces* **2015**, *7*, 27432−27439.

(37) Jeong, Y. R.; Park, H.; Jin, S. W.; Hong, S. Y.; Lee, S.-S.; Ha, J. S. Highly Stretchable and Sensitive Strain Sensors Using Fragmentized Graphene Foam. *Adv. Funct. Mater.* **2015**, *25*, 4228−4236.

(38) Qin, Y.; Peng, Q.; Ding, Y.; Lin, Z.; Wang, C.; Li, Y.; Xu, F.; Li, J.; Yuan, Y.; He, X.; Li, Y. Lightweight, Superelastic, and Mechanically Flexible Graphene/Polyimide Nanocomposite Foam for Strain Sensor Application. *ACS Nano* **2015**, *9*, 8933−8941.

(39) Liu, Q.; Chen, J.; Li, Y.; Shi, G. High-Performance Strain Sensors with Fish-Scale-Like Graphene-Sensing Layers for Full-Range Detection of Human Motions. *ACS Nano* **2016**, *10*, 7901−7906.

(40) Wang, C.; Li, X.; Gao, E.; Jian, M.; Xia, K.; Wang, Q.; Xu, Z.; Ren, T.; Zhang, Y. Carbonized Silk Fabric for Ultrastretchable, Highly Sensitive, and Wearable Strain Sensors. *Adv. Mater.* **2016**, *28*, 6640−6648.

(41) Mattmann, C.; Clemens, F.; Troster, G. Sensor for Measuring Strain in Textile. *Sensors* **2008**, *8*, 3719−3732.

(42) Muth, J. T.; Vogt, D. M.; Truby, R. L.; Menguc, Y.; Kolesky, D. B.; Wood, R. J.; Lewis, J. A. Embedded 3D Printing of Strain Sensors within Highly Stretchable Elastomers. *Adv. Mater.* **2014**, *26*, 6307−6312.

(43) Kim, K. K.; Hong, S.; Cho, H. M.; Lee, J.; Suh, Y. D.; Ham, J.; Ko, S. H. Highly Sensitive and Stretchable Multidimensional Strain Sensor with Prestrained Anisotropic Metal Nanowire Percolation Networks. *Nano Lett.* **2015**, *15*, 5240−7.

(44) Kim, K. K.; Hong, S.; Cho, H. M.; Lee, J.; Suh, Y. D.; Ham, J.; Ko, S. H. Highly Sensitive and Stretchable Multidimensional Strain Sensor with Prestrained Anisotropic Metal Nanowire Percolation Networks. *Nano Lett.* **2015**, *15*, 5240−5247.

https://doi.org/10.1021/acsnano.1c07645
ACS Nano 2022, 16, 541−553

(45) Xiao, X.; Yuan, L. Y.; Zhong, J. W.; Ding, T. P.; Liu, Y.; Cai, Z. X.; Rong, Y. G.; Han, H. W.; Zhou, J.; Wang, Z. L. High-Strain Sensors Based on ZnO Nanowire/Polystyrene Hybridized Flexible Films. *Adv. Mater.* **2011**, *23*, 5440−5444.
(46) Su, Y. W.; Ping, X. C.; Yu, K. J.; Lee, J. W.; Fan, J. A.; Wang, B.; Li, M.; Li, R.; Harburg, D. V.; Huang, Y. A.; Yu, C. J.; Mao, S. M.; Shim, J.; Yang, Q. L.; Lee, P. Y.; Armonas, A.; Choi, K. J.; Yang, Y. C.; Paik, U.; Chang, T.; et al. In-Plane Deformation Mechanics for Highly Stretchable Electronics. *Adv. Mater.* **2017**, *29*, 1604989.
(47) Timoshenko, S. *Strength of Materials*; D. Van Nostrand Company, Inc.: New York, 1930.
(48) Holzapfel, G. A. *Nonlinear Solid Mechanics: A Continuum Approach for Engineering*; Wiley: Chichester, New York, 2000.
(49) Son, D.; Kang, J.; Vardoulis, O.; Kim, Y.; Matsuhisa, N.; Oh, J. Y.; To, J. W. F.; Mun, J. W.; Katsumata, T.; Liu, Y. X.; McGuire, A. F.; Krason, M.; Molina-Lopez, F.; Ham, J.; Kraft, U.; Lee, Y.; Yun, Y.; Tok, J. B. H.; Bao, Z. N. An Integrated Self-Healable Electronic Skin System Fabricated via Dynamic Reconstruction of a Nanostructured Conducting Network. *Nat. Nanotechnol.* **2018**, *13*, 1057−1065.
(50) Boutry, C. M.; Kaizawa, Y.; Schroeder, B. C.; Chortos, A.; Legrand, A.; Wang, Z.; Chang, J.; Fox, P.; Bao, Z. N. A Stretchable and Biodegradable Strain and Pressure Sensor for Orthopaedic Application. *Nat. Electron.* **2018**, *1*, 314−321.